The Astrophysical Journal, 970:46 (9pp), 2024 July 20 https://doi.org/10.3847/1538-4357/ad5543
© 2024. The Author(s). Published by the American Astronomical Society.
OPEN ACCESS

A Model for Pair Production Limit Cycles in Pulsar Magnetospheres

Takuya Okawa and Alexander Y. Chen
Physics Department and McDonnell Center for the Space Sciences, Washington University in St. Louis, MO 63130, USA; o.takuya@wustl.edu
Received 2024 April 12; revised 2024 June 5; accepted 2024 June 5; published 2024 July 16

Abstract

It was recently proposed that the electric field oscillation as a result of self-consistent $e^{\pm}$ pair production may be the source of coherent radio emission from pulsars. Direct particle-in-cell simulations of this process have shown that the screening of the parallel electric field by this pair cascade manifests as a limit cycle, as the parallel electric field is recurrently induced when pairs produced in the cascade escape from the gap region. In this work, we develop a simplified time-dependent kinetic model of $e^{\pm}$ pair cascades in pulsar magnetospheres that can reproduce the limit-cycle behavior of pair production and electric field screening. This model includes the effects of a magnetospheric current, the escape of $e^{\pm}$, as well as the dynamic dependence of pair production rate on the plasma density and energy. Using this simple theoretical model, we show that the power spectrum of electric field oscillations averaged over many limit cycles is compatible with the observed pulsar radio spectrum.

Unified Astronomy Thesaurus concepts: Radio pulsars (1353); Plasma astrophysics (1261); Neutron stars (1108); Radio sources (1358)

1. Introduction

Pulsars are rapidly rotating, highly magnetized neutron stars that produce coherent radio emission with enormous brightness temperature (see, e.g., Philippov & Kramer 2022, for a review). Very quickly after its discovery, it was realized that the magnetic field near the surface of a pulsar can be strong enough to initiate a QED $e^{\pm}$ pair cascade (Sturrock 1971). It was believed that pulsars can fill their surroundings with plasma through this $e^{\pm}$ pair production process, screening the electric field $E_{\parallel}$ along the magnetic field and creating a smooth force-free magnetosphere (Contopoulos et al. 1999; Spitkovsky 2006). The regions in the magnetosphere with unscreened $\boldsymbol{E} \cdot \boldsymbol{B}$ are called "gaps" and they are the main locations for pair production activity (see, e.g., Ruderman & Sutherland 1975; Arons 1983; Cheng et al. 1986).

Arguably, the most important pair-producing gap is located at the pulsar's polar cap, since it supplies the plasma on open field lines that is believed to be the source of coherent radio emission (Sturrock 1971). Beloborodov (2008) demonstrated theoretically that the pair production process at the polar cap must be inherently time-dependent when the magnetospheric current is spacelike, and Levinson et al. (2005) showed that this process tends to produce large-amplitude oscillations of the accelerating electric field. Numerical simulations performed by Timokhin (2010) demonstrated such oscillations from first principles, and showed that pair production happens in quasiperiodic bursts. Subsequent 1D and 2D particle-in-cell (PIC) simulations all showed the limit-cycle behavior of the pair production process (e.g., Timokhin & Arons 2013; Cruz et al. 2021), and it was proposed that this pair production oscillation may directly produce coherent radio waves (Philippov et al. 2020). A better understanding of the $e^{\pm}$ discharge physics may help us finally solve the decades-old puzzle of the origin of pulsar radio emission.

Original content from this work may be used under the terms of the Creative Commons Attribution 4.0 licence. Any further distribution of this work must maintain attribution to the author(s) and the title of the work, journal citation and DOI.

Recently, it was also realized that the intense parallel electric field in the gap region may be the strongest source of persistent oscillatory $\boldsymbol{E} \cdot \boldsymbol{B}$ in the Universe. Pseudoscalar particles such as QCD axions interact with the electromagnetic sector through their coupling to $\boldsymbol{E} \cdot \boldsymbol{B}$; therefore the spark gaps in the pulsar magnetosphere may be one of the most promising regions for producing these axion-like particles (ALPs; Prabhu 2021). The QCD axions and ALPs are physically motivated and form a popular class of dark matter candidates (Abbott & Sikivie 1983; Dine & Fischler 1983; Preskill et al. 1983). Recent work by Noordhuis et al. (2023) used the pair cascade process at pulsar polar caps to derive novel constraints on axion signals. A better understanding of the complex plasma physics behind $e^{\pm}$ pair cascade oscillations may be able to further improve the existing constraints on axion properties.

Driven by the need to explain pulsar radio emission, semianalytic models motivated by first-principles simulations have been constructed recently (Cruz et al. 2021; Tolman et al. 2022). These models improved over the work by Levinson et al. (2005) by taking into account kinetic effects. However, no single semianalytic model so far can properly reproduce the limit-cycle behavior of the pair cascade process, which includes the growth of the inductive electric field and its subsequent screening from pair production. Numerical simulations, on the other hand, are extremely expensive when the full QED cascade physics is taken into account, and it is impossible to simulate the parameter regime of realistic pulsars in 2D or 3D with current computational capabilities.

In this paper, we attempt to construct a minimal time-dependent theoretical model that can reproduce all salient features of the pulsar $e^{\pm}$ pair cascade process. This model takes into account the highly relativistic and nonlinear plasma physics governing the pair plasma near the pulsar polar cap, and uses a physically motivated prescription to incorporate pair production and escape. In Section 2, we outline this theoretical model and derive the differential equations governing it. In Section 3, we discuss our choice of the pair production source term in the equations and compare a few different alternatives. In Section 4, we present numerical solutions to this model and discuss their parameter dependence. Finally, in Section 5 we

discuss the observational implications and how this model can be improved in the future.

2. Theoretical Model

2.1. Equations and Closure

We start from the coupled Vlasov–Maxwell system in 1D, along the local magnetic field, with a source term for pair production. Using x to denote the coordinate along the field line, the system reads

$$\frac{\partial E}{\partial t} = c(\nabla \times \boldsymbol{B})_{\parallel} - 4\pi j \tag{1}$$

$$\frac{\partial f_{\pm}}{\partial t} = -v\frac{\partial f_{\pm}}{\partial x} - q_{\pm}E\frac{\partial f_{\pm}}{\partial p} + S_{\pm}, \tag{2}$$

where $\pm$ denotes the electron or positron species, and $S_{\pm}$ is the source term due to $e^{\pm}$ pair production. Assuming the magnetic field is static and does not couple to the dynamics in the spark gap, we write $j_B = c(\nabla \times \boldsymbol{B})_{\parallel}/4\pi$. Ampère's law becomes

$$\frac{\partial E}{\partial t} = 4\pi(j_B - j). \tag{3}$$

The electric current density j in Equation (3) can be computed directly from the distribution function:

$$j = \sum_{s=\pm} q_s \int v f_s \, dp. \tag{4}$$

Taking the time derivative of the current and using the Vlasov Equation (2), we can write down the evolution equation for j:

$$\begin{aligned}\frac{\partial j}{\partial t} &= \sum_{s=\pm} q_s \int v \frac{\partial f_s}{\partial t} \, dp \\ &= \sum_{s=\pm} q_s \int v\left(-v\frac{\partial f_s}{\partial x} - q_s E\frac{\partial f}{\partial p} + S_s\right)dp \\ &= \sum_{s=\pm} \int \left[q_s v\left(-v\frac{\partial f_s}{\partial x} + S_s\right) + q_s^2 E f_s \frac{dv}{dp}\right] dp,\end{aligned} \tag{5}$$

where we have used integration by parts to move ∂_p onto v. Since $dv/dp = 1/m\gamma^3$, the last term can be written as

$$\int q_s^2 E f_s \frac{dv}{dp} \, dp = \frac{q_s^2 E n_s}{m}\left\langle \frac{1}{\gamma_s^3}\right\rangle, \tag{6}$$

where $n_s = \int f_s dp$ is the number density of the particle species, and the angular bracket means taking the expectation value with respect to the distribution function.

Our goal is to construct a set of coupled time-dependent ordinary differential equations that can be solved numerically. Therefore, we specialize to one point in space where particle acceleration, pair production, and electric field screening are happening, similar to the approach adopted by Cruz et al. (2021) and Tolman et al. (2022). To this end, we postulate a macroscopic length scale L for the variation of plasma density and approximate the spatial derivative as $\partial_x \sim 1/L$. We further assume that pairs flow away from the point of interest at the speed of light, $v \approx c$. The Vlasov equation then becomes

$$\frac{\partial f_{\pm}}{\partial t} = -\frac{c}{L}f_{\pm} - qE\frac{\partial f_{\pm}}{\partial p} + S_{\pm}. \tag{7}$$

This is our attempt to approximately model the effect of plasma escape. Using this approximation, the time evolution Equation (5) for the current becomes

$$\frac{\partial j}{\partial t} = -\frac{c}{L}j + \sum_{s=\pm}\frac{q_s^2 E n_s}{m}\left\langle \frac{1}{\gamma_s^3}\right\rangle - q_s\int v S_s \, dp. \tag{8}$$

Two extra quantities appear in Equation (8): the number density of each species $n_{\pm}$ and the expectation value of $1/\gamma^3$ for each species. The time evolution of $n_{\pm}$ can be written down by simply integrating the Vlasov Equation (7) over the momentum space:

$$\frac{\partial n_{\pm}}{\partial t} = -\frac{c}{L}n_{\pm} + \int S_{\pm} \, dp. \tag{9}$$

However, the $\langle 1/\gamma^3\rangle$ term requires an additional equation for closure, which invariably involves higher moments of the distribution function. In this paper, we make the simplest hydrodynamic approximation, $\langle 1/\gamma^3\rangle \approx 1/\langle\gamma\rangle^3$, and use $\langle p_{\pm}\rangle$ for closure by computing $\langle\gamma_{\pm}\rangle = \sqrt{1 + \langle p_{\pm}\rangle^2/m^2c^2}$. Additional discussion about this choice is included in Appendix A, where we outline a systematic way to improve this approximation. Similar to the current Equation (8), the time evolution of $\langle p_{\pm}\rangle$ can be obtained by substituting the Vlasov equation and Equation (9), and then using integration by parts:

$$\begin{aligned}\frac{\partial\langle p_{\pm}\rangle}{\partial t} &= \frac{1}{n_{\pm}}\int p\frac{\partial f_{\pm}}{\partial t} \, dp - \frac{\dot{n}_{\pm}}{n_{\pm}}\langle p_{\pm}\rangle \\ &= \tfrac{1}{n_{\pm}}\int S_{\pm}(p_{\pm} - \langle p_{\pm}\rangle)dp + q_{\pm}E.\end{aligned} \tag{10}$$

Equations (8)–(10) involve an integral of the pair production source term S, which we have not specified. In this paper, we assume all pairs are produced at a single energy, but the pair production rate may be a general function of E, $n_{\pm}$, and $\langle p_{\pm}\rangle$, in order to take into account the feedback from electric field screening:

$$S_+ = S_- = S(E, n_{\pm}, \langle p_{\pm}\rangle)\delta(p - p_{\rm pair}). \tag{11}$$

We will discuss our specific choices for the function S in Section 3. Since electrons and positrons are accelerated in opposite directions in the gap, the pairs produced from γ-ray photons emitted by them have opposite momenta. In addition, the pairs produced from curvature radiation emitted from primary particles have much lower energies than the accelerated electrons and positrons. Therefore we set $p_{\rm pair} = 0$ in this model, which significantly simplifies the integrals of the source term.

2.2. Numerical Units

In order to solve the coupled Equations (3), (8), (9), and (10) together numerically, we introduce a unit system that is motivated by the physics at the pulsar polar cap. In the rest of this paper, dimensionless variables are expressed with tildes, and their units are expressed with the subscript 0, e.g., $\tilde{x} \equiv x/x_0$.

We normalize the electron and positron densities $n_\pm$ with the Goldreich–Julian density (Goldreich & Julian 1969):

$$n_{\rm GJ} = \frac{\boldsymbol{B}\cdot\boldsymbol{\Omega}_{\rm NS}}{2\pi ec} \simeq 6.9\times 10^{10}\left(\frac{B}{10^{12}{\rm G}}\right)\left(\frac{1{\rm s}}{P}\right){\rm cm}^{-3}, \quad (12)$$

where B is the local magnetic field strength, and Ω is the angular rotation frequency of the neutron star. The units of length and time are determined by the plasma frequency associated with $n_{\rm GJ}$:

$$\omega_0^2 = \frac{4\pi n_{\rm GJ}e^2}{m_e}. \quad (13)$$

We then set the unit of time to be $t_0 \equiv 1/\omega_0$ and the unit of length to be $x_0 \equiv c/\omega_0$. Using the nominal value of $n_{\rm GJ}$, our length unit is close to $x_0 \approx 2$ cm. Note that the real plasma frequency after pair production sets in is going to be significantly higher, and this ω_0 simply sets a lower bound for the plasma frequency.

For electron momentum, we set $p_0 \equiv m_e c$, and the dimensionless momentum is simply $\tilde{p} = \gamma\beta$. The unit of the electric field $E_0 \equiv mc/et_0$ is then determined as the strength of the electric field that increases $\tilde{p} = \gamma\beta$ by 1 in the unit time t_0. The unit electric current density $j_0 \equiv en_{\rm GJ}c$ is equivalent to $j_0 \equiv E_0/4\pi t_0$ due to our choice of t_0. Lastly, we define the units of the electron distribution function and pair production rate as $f_0 \equiv n_{\rm GJ}/p_0$ and $S_0 \equiv f_0/t_0$, respectively. In summary, our choice of units is listed below:

$$\begin{aligned} &t_0 \equiv (4\pi e^2 n_{\rm GJ}/m_e)^{-1/2} \approx 6.7\times 10^{-11}\,{\rm s}\\ &p_0 \equiv m_e c,\ \ n_0 \equiv n_{\rm GJ},\ \ E_0 \equiv mc/et_0\\ &j_0 \equiv en_{\rm GJ}c,\ \ f_0 \equiv n_{\rm GJ}/p_0,\ S_0 \equiv f_0/t_0. \end{aligned} \quad (14)$$

After incorporating the source term (11) and using the units listed above, these are the equations that we solve numerically:

$$\frac{d\tilde{E}}{d\tilde{t}} = \tilde{j}_B - \tilde{j}, \quad (15)$$

$$\frac{d\tilde{j}}{d\tilde{t}} = -\frac{\tilde{j}}{\tilde{L}} + \sum_{s=\pm}\left\langle\frac{1}{\gamma_s^3}\right\rangle\tilde{E}\tilde{n}_s, \quad (16)$$

$$\frac{d\tilde{n}_\pm}{d\tilde{t}} = -\frac{\tilde{n}_\pm}{\tilde{L}} + \tilde{S}(\tilde{E},\tilde{n}_\pm,\langle\tilde{p}_\pm\rangle), \quad (17)$$

$$\frac{d\langle\tilde{p}_\pm\rangle}{d\tilde{t}} = -\frac{\tilde{S}(\tilde{E},\tilde{n}_\pm,\langle\tilde{p}_\pm\rangle)}{\tilde{n}_\pm}\langle\tilde{p}_\pm\rangle + \frac{q_\pm}{e}\tilde{E}. \quad (18)$$

Apart from the pair production source function $\tilde{S}$ to be discussed in Section 3, there are two dimensionless parameters in this model, $\tilde{L}$ and $\tilde{j}_B$. The length scale $\tilde{L}$ parameterizes plasma escape and will be taken to be approximately of the same order as the polar cap size $r_{\rm pc}$. The magnetospheric current $\tilde{j}_B$ provides a driving term for the electric field and is responsible for its growth after the pair plasma has advected away. We typically take j_B to be a few times $en_{\rm GJ}c$, which is consistent with the magnetospheric current near the polar cap seen in global force-free and PIC simulations (see, e.g., Bai & Spitkovsky 2010; Gralla et al. 2017).

Combining Equations (15) and (16), the equation for $\tilde{E}$ is essentially a damped oscillator with a constant forcing term:

$$\frac{d^2\tilde{E}}{d\tilde{t}^2} + \frac{1}{\tilde{L}}\frac{d\tilde{E}}{d\tilde{t}} + \sum_{s=\pm}\tilde{n}_s\left\langle\frac{1}{\gamma_s^3}\right\rangle\tilde{E} = \frac{\tilde{j}_B}{\tilde{L}}. \quad (19)$$

We define the effective frequency of the oscillation:

$$\bar{\omega}^2 = \sum_{s=\pm}\tilde{n}_s\left\langle\frac{1}{\gamma_s^3}\right\rangle. \quad (20)$$

The growth and screening of the electric field depend on the value of this effective frequency. Initially, when $\bar{\omega}$ is very small, the particular solution to the equation is linear growth, $\tilde{E} \propto \tilde{j}_B\tilde{t}$. As the electric field increases, the plasma is accelerated and pair production sets in, which increases $\bar{\omega}$. The nature of the solution changes when $\bar{\omega}$ becomes large enough to start oscillations, which initiates the electric field screening phase.

Equation (19) also shows that the evolution of $\tilde{E}$ and $\tilde{j}$ somewhat separates from the other two equations, and the plasma properties only affect the effective frequency in the particular combination of Equation (20). This provides some robustness to the model, which separates the dynamics of the electric field from the detailed microphysics model we use for pair production.

3. Modeling the Pair Production Source Term

The main goal of this paper is to construct a self-contained theoretical model that can reproduce the limit-cycle behavior of $e^\pm$ pair production. To achieve this goal, we need to find a suitable function S in Equation (11). The pair cascade process is a complicated (and potentially nonlocal) sequence of curvature radiation, synchrotron radiation, and magnetic pair production or photon–photon annihilation. Although numerical simulations have succeeded in describing these processes accurately, it is impossible to include their full effects in a zero-dimensional model. Therefore, we try to find a simple qualitative source function using a trial-and-error process.

Since the source function S may generally depend on $\tilde{E}$, $\tilde{n}_\pm$, and $\langle p_\pm\rangle$, we experimented with a number of different types of functional forms (in all cases g is a dimensionless parameter):

(i) Constant pair production rate: $\tilde{S} = g$;
(ii) Proportional to plasma density: $\tilde{S} = g\sum_s \tilde{n}_s$;
(iii) Proportional to average momentum: $\tilde{S} = g\sum_s|\langle\tilde{p}_s\rangle|$;
(iv) Proportional to local electric field: $\tilde{S} = g|\tilde{E}|$;
(v) Proportional to electric field and plasma density: $\tilde{S} = g|\tilde{E}|\sum_s\tilde{n}_s$;
(vi) Proportional to average momentum and plasma density: $\tilde{S} = g\sum_s\tilde{n}_s|\langle\tilde{p}_s\rangle|$.

Type (i), a constant pair production rate, is similar to the pair production function used by Tolman et al. (2022). Since it does not allow for any feedback from the evolution of $\tilde{E}$ and $\langle\tilde{p}\rangle$, we expect the gap to be screened and never grow again. It is a good choice for studying the screening phase, but we do not expect it to lead to a limit cycle. Similarly, type (ii) only depends on the plasma density, and we expect the electric field will not grow again after the initial screening phase. The other four types of pair production function take into account feedback from the field evolution in different ways, and it is not immediately obvious which one leads to a limit-cycle behavior.

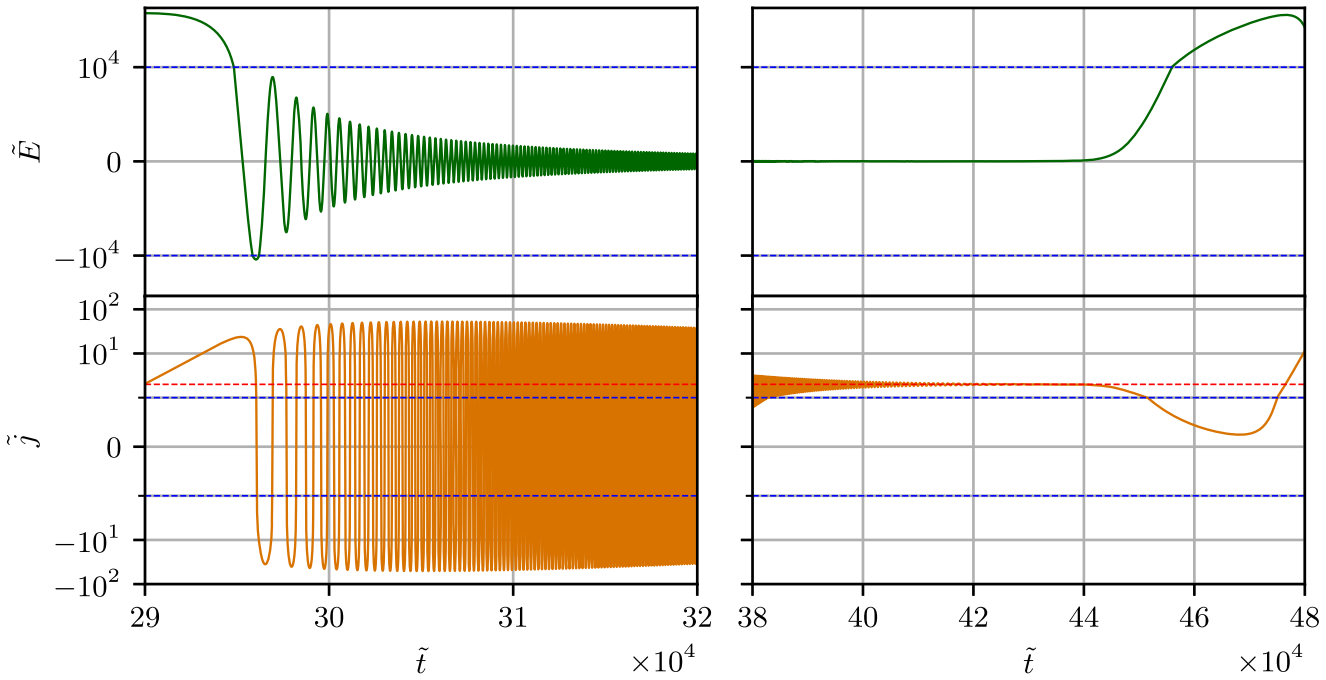

Figure 1. A zoomed-in plot of the time evolution of the electric field and the charged current in "symlog" scale, with a blue dotted line showing the threshold between linear and logarithmic scales. Left and right columns show the beginning of the screening phase and the transition to the next phase of electric field growth, respectively. The escape length scale $\tilde{L}$ is set as $\tilde{L} = 10^4$, and the pair production parameter is $g = 10^{-11}$. The value of $\tilde{j}_B$ is chosen to be 2 and is shown as red dotted lines.

Note that we have not included a source function type that involves a pair production threshold $\gamma_{\rm thr}$, as was done by Levinson et al. (2005) and Cruz et al. (2021). We found that since Equations (15)–(18) are already quite stiff, a threshold condition often leads to discontinuous transitions that can easily cause the solutions to run away. A more physical justification is that, since Equation (18) evolves the average momentum that exponentially decreases when pair production sets in, it is not appropriate to use a threshold condition on this value directly. An additional function that tracks the energies of primary particles in the gap may be better suited for applying the threshold condition, but we will leave the experimentation of such a model to future works.

After extensive experimentation, we found that the only source function that can consistently reproduce the pair discharge limit-cycle behavior is type (vi), where $\tilde{S}$ is proportional to both the plasma density and the average particle momentum. A solution with this type of source function is plotted in Figure 1, which depicts different parts of one pair discharge cycle. We will discuss this solution and its parameter dependence in Section 4.

We believe this model successfully captures the limit-cycle behavior for two main reasons: (i) if the source function does not depend on the number density $\tilde{n}_\pm$, then from Equation (17), $\tilde{n}_\pm$ tends to relax to a constant value exponentially; (ii) this model has a built-in feedback mechanism in that $\tilde{S} \propto \langle p_\pm \rangle$, which allows pair production to respond to particle acceleration (or lack thereof). More discussion about how other models fail is included in Appendix B.

Coincidentally, type (vi) of the source function is applicable to pairs produced by curvature photons, which may be the primary channel for pair production at pulsar polar caps. The energy loss rate of an electron of Lorentz factor γ undergoing curvature radiation is (see, e.g., Jackson 1999)

$$P_{\rm CR} = \frac{2}{3}\frac{e^2 c}{\rho_c^2}\gamma^4, \tag{21}$$

where ρ_c is the field line curvature radius. The characteristic photon energy from curvature radiation is

$$\epsilon_{\rm CR} = \frac{3}{2}\frac{\lambda\!\!\!^{-}}{\rho_c}\gamma^3 m_e c^2, \tag{22}$$

where $\lambda\!\!\!^{-}$ is the reduced electron Compton wavelength. Therefore, the number of curvature photons $n_{\rm CR} \sim P_{\rm CR}/\epsilon_{\rm CR}$ emitted by an ultrarelativistic primary electron per unit time scales as γ, and each photon converts to an $e^\pm$ pair. Additional synchrotron cascade may increase the total number of pairs produced by a single primary electron (Daugherty & Harding 1983), but it is a reasonable first approximation to set the pair production rate to be proportional to $n_\pm \gamma_\pm$, which is our source function type (vi).

This correspondence to curvature radiation is also our way to choose the numerical parameter g in the expression of the source function. The constant g has the physical meaning of number of pairs produced per time t_0 per primary particle, divided by its Lorentz factor:

$$\begin{aligned} g &= \frac{P_{\rm CR}}{\epsilon_{\rm CR}}\frac{t_0}{\gamma} = \frac{4}{9}\frac{e^2}{\lambda\!\!\!^{-}\rho_c m_e c} t_0 \\ &\approx 6.5 \times 10^{-11}\left(\frac{\rho_c}{10^8\ {\rm cm}}\right)^{-1} B_{12}^{-1/2} P_1^{1/2}, \end{aligned} \tag{23}$$

where $B_{12} = B/10^{12}$ G and $P_1 = P/1$ s. For our reference model in Section 4, we use $g = 10^{-11}$.

4. Numerical Solutions and Parameter Dependence

We solve the set of six coupled ordinary differential equations (15)–(18) using the Python library function `scipy.integrate.solve\inferior_ivp`. Anticipating a stiff set of equations, we use the library-provided "Radau" method, which is an implicit Runge–Kutta method of the Radau IIA family of order 5 (Hairer et al. 1993). Since the method is adaptive, the results are interpolated through a cubic polynomial to a dense output array of at least 500,000 points, which allows for fast Fourier transform calculations to analyze the power spectrum of electric field oscillations.

There are only three numerical parameters in this model. $\tilde{j}_B$ is the magnetospheric current in units of $en_{\rm GJ}c$, which is usually of order unity at pulsar polar caps. Note that although we normalize plasma density with $n_{\rm GJ}$, the system mainly operates in the regime of $\rho \sim 0$ and the current is therefore always spacelike. $\tilde{L}$ is the dimensionless parameter that roughly characterizes the size of the pair-producing region and controls how quickly plasma escapes from the region. We take it to be comparable to or smaller than the radius of the pulsar polar cap. The constant g in the source function S parameterizes the pair production rate, and we use curvature radiation for typical pulsar parameters to choose its value in our reference model, as discussed in Section 3.

Figure 1 shows the evolution of electric field $\tilde{E}$ and current density $\tilde{j}$ over time for a particular set of parameters. Initially, the system is filled with $n_+ = n_- = n_{\rm GJ}$ with both species at rest. The electric field E and electric current j are initially also zero. Due to the magnetospheric current j_B, the electric field starts to grow linearly with time, accelerating both species of charges. Electron–positron pairs are continuously produced during this time, exponentially increasing the number densities $n_\pm$. Electric field screening happens when the effective frequency $\bar{\omega} = \sqrt{\sum \tilde{n}_s \langle 1/\gamma_s^3 \rangle}$ becomes large enough, $\bar{\omega} \gtrsim 1/\tilde{L}$. This is when the solution transitions to an oscillatory nature, at which point the electric field screening is well described by a weakly damped oscillator with slowly changing frequency. The damping effect drives the electric field to 0 and the electric current to $\tilde{j}_B$. The electric field grows again when the plasma exits the region and the effective frequency drops far below $1/\tilde{L}$.

Figure 2 shows the full solution for three models with different pair production parameters g. The electric field growth and screening limit cycle are observed in all three cases. However, the three models differ in their maximum electric field strength $E_{\rm max}$, the quasi-period of the limit cycle, and the maximum effective frequency $\bar{\omega}_{\rm max}$. We see that a lower pair production efficiency leads to a larger $E_{\rm max}$ in the gap, and the electrons and positrons are accelerated to much higher maximum energies. The maximum effective frequency for electric field oscillations $\bar{\omega}_{\rm max}$ is also lower when pair production is less efficient, due to the much higher plasma Lorentz factors.

One interesting feature of this model is that, even though $\tilde{j}$ changes sign rapidly as the electric field is screened, the mean momentum $\langle p_\pm \rangle$ just decreases but never changes sign again. We believe this is physical, as $\langle p_\pm \rangle$ can be dominated by a population of high-energy particles, while these particles do not contribute as much to $\langle \beta_\pm \rangle$. As a result, the current density can become close to zero and change sign due to large numbers of pairs being produced. Note that $|\langle p_+ \rangle|$ and n_+ are completely symmetric with $|\langle p_- \rangle|$ and n_- in all solutions. This is simply a consequence of the symmetry $n_+ \leftrightarrow n_-$ and $\langle p_+ \rangle \leftrightarrow -\langle p_- \rangle$ in Equations (17) and (18).

Another feature of the model is that it predicts an extremely high pair multiplicity of $n_\pm/n_{\rm GJ} \gtrsim 10^{16}$, far greater than previous more rigorous studies (e.g., Timokhin & Harding 2019). This is a limitation of the model that stems from our choice of closure, where $\langle 1/\gamma_\pm \rangle \sim 1/\langle \gamma_\pm \rangle^3$, as well as the very simplified pair production source function discussed in Section 3. Our hydrodynamic closure may be reasonable during the phase of electric field growth, where all particles are accelerated together, but it significantly underestimates this value when pair production is significant. Since electric field screening is controlled by the effective frequency $\bar{\omega}$, the system develops an unreasonably high plasma density to compensate. Experimentation with higher-order closures shows that a better estimate of $\langle 1/\gamma^3 \rangle$ does tend to reduce the number density (see Appendix A). Our source term for pair production is also quite crude, therefore we believe the model should not be used to directly study the pair multiplicities from pair cascades at pulsar polar caps.

Figure 3 illustrates the dependence of the electric field solution on initial conditions and other numerical parameters. Experimenting with significantly different initial conditions, we find that the initial condition does not affect the later recurrent behavior of the solution, as all initial conditions are attracted to the same limit cycle. Different initial electric fields and number densities of charged particles just result in different times of onset of the electric field screening.

On the other hand, the different choices of parameters lead to the different time evolutions of the electric field. The growth rate of the electric field before its screening is only governed by $\tilde{j}_B$, as that part of the solution is described by $\tilde{E} \propto \tilde{j}_B \tilde{t}$. Systems with larger $\tilde{j}_B$ or g start screening the electric fields at earlier times, as pair production becomes more efficient in both cases. $\tilde{L}$ describes how slowly or quickly charged particles escape from the pair-producing region, and thus a smaller $\tilde{L}$ leads to an increased duty cycle for the gap. This is because when pairs escape more quickly, the system spends less time before the electric fields start growing again.

This oscillating electric field in the polar cap has been suggested as a possible origin for coherent radio emission from pulsars (Philippov et al. 2020). If this is the case, then the frequency spectrum of electric field oscillations should be directly related to the resulting radio waves. Figure 4 shows the power spectrum of the electric field energy for the three models that were shown in Figure 2. The spectrum generally follows a power law, but it has a cutoff that scales with the pair production parameter g. This cutoff is located near the maximum $\bar{\omega}$, which is physically the maximum oscillation frequency of the electric field. The spectrum beyond this cutoff arises purely due to interpolation onto a dense output grid. The cutoff frequency is higher for models with more efficient pair production. For higher values of g, the frequency range contains what is typically observed in pulsar radio emission.

Compared to the frequency cutoff, we find that the power law index is only weakly dependent on the model parameters, and all indices lie within the 1.8–2.0 range. This is largely compatible with the observed pulsar radio emission spectra of $\omega^{-1.4\pm1.0}$ (Bates et al. 2013). However, even within one single model, the spectral index seems to vary over the frequency range. More detailed modeling of the escape of these

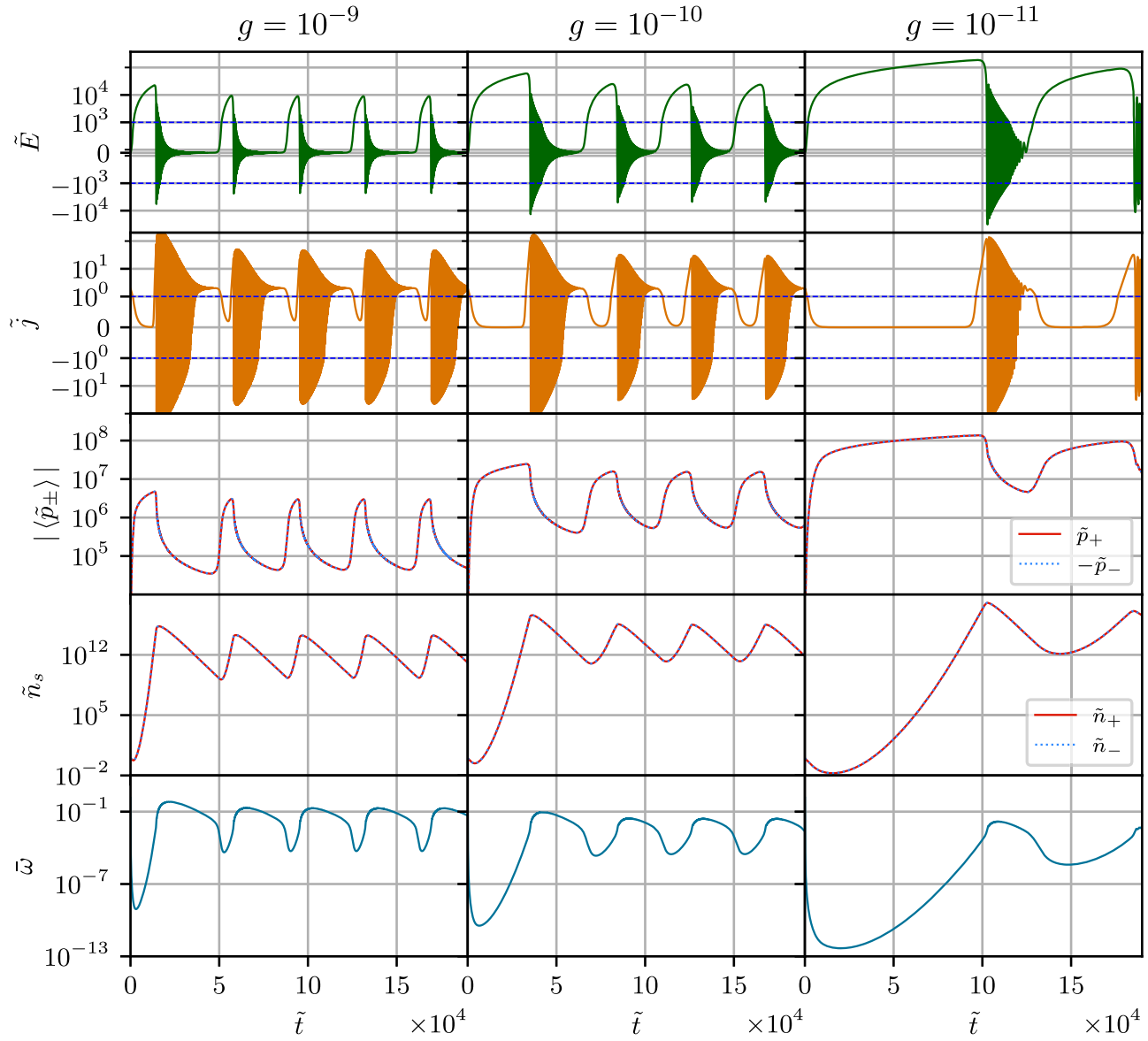

Figure 2. Full solution of Equations (15)–(18) (from top to bottom: $\tilde{E}$, $\tilde{j}$, $|\langle\tilde{p}_\pm\rangle|$, $\tilde{n}_\pm$, and effective frequency $\bar{\omega}$) as a function of $\tilde{t}$. The first two rows are plotted in "symlog" scale and blue dashed lines denote the transition from linear to logarithmic scales. Each column assumes a different production rate of charged particles in pair cascades; $g = 10^{-9}$, $g = 10^{-10}$, and $g = 10^{-11}$ are chosen for the left, central, and right columns, respectively. Initial conditions and model parameters are chosen as $\tilde{E}_{\rm init} = \tilde{j}_{\rm init} = \langle\tilde{p}_\pm\rangle_{\rm init} = 0$, $\tilde{n}_{\pm,{\rm init}} = 1$, $\tilde{j}_B = 2$, and $\tilde{L} = 2 \times 10^3$. The production rate of charged particles is set to be $\tilde{S} = g\sum_\pm \tilde{n}_\pm |\langle\tilde{p}_\pm\rangle|$.

oscillations as coherent electromagnetic waves is required to make definitive predictions about the radio emission spectrum.

5. Summary and Discussion

We have presented a minimal time-dependent theoretical model that captures the limit-cycle behavior of the $e^\pm$ production process at the pulsar polar cap. The model has only three parameters and reproduces correctly the complete pair discharge cycle, from the induction to the screening of $E_\parallel$. The solution is agnostic of initial conditions and always settles to the same recurrent behavior under the same parameters, as is characteristic of a true limit cycle. We explored the parameter dependence of the model and computed the power spectrum of the electric field oscillations. We found that the spectral index is around 1.8–2.0, weakly dependent on model parameters within the range we have experimented with. This result is largely compatible with the range of spectral indices of observed pulsar radio emission.

In addition, the frequency range of the oscillations seems to be compatible with the observed range from 100 MHz to several GHz. The high-frequency cutoff of the power spectrum depends sensitively on the efficiency of pair production and becomes lower when pair production is less efficient. This dependence may provide an alternative explanation of the pulsar death line. As a pulsar spins down, its polar cap potential drops, which decreases the pair production efficiency. This results in an overall reduction of the high-frequency cutoff of its radio spectrum, rendering it undetectable by our radio telescopes, which are sensitive between 100 MHz and a few GHz.

Although the three numerical parameters in this model have straightforward physical meanings, their values need to be fine-tuned by comparing the model with first-principles PIC simulations such as those by Timokhin & Arons (2013) and

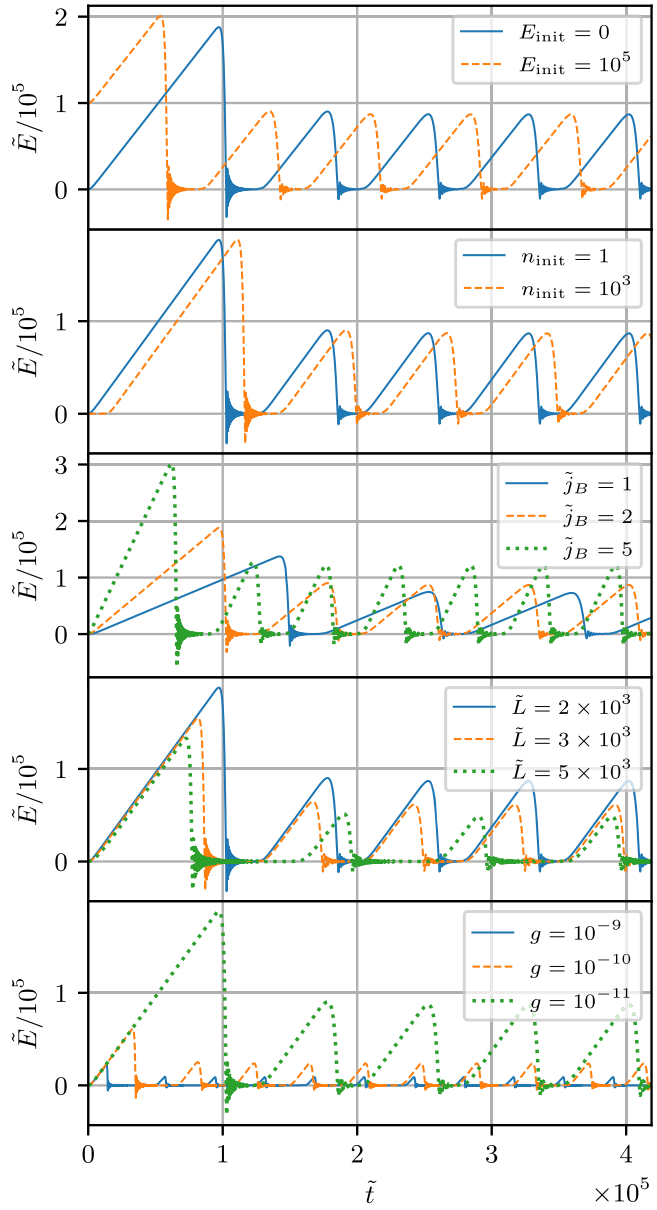

Figure 3. Plots of electric fields with different choices of one of the initial conditions or parameters. From top to bottom, each plot compares the behavior of electric fields with several choices of $\tilde{E}_{\rm init}$, $\tilde{n}_{\rm init}$, $\tilde{j}_B$, $\tilde{L}$, and g, respectively. The reference model used for comparison is $\tilde{j}_B = 2$, $\tilde{L} = 2 \times 10^3$, and $g = 10^{-11}$.

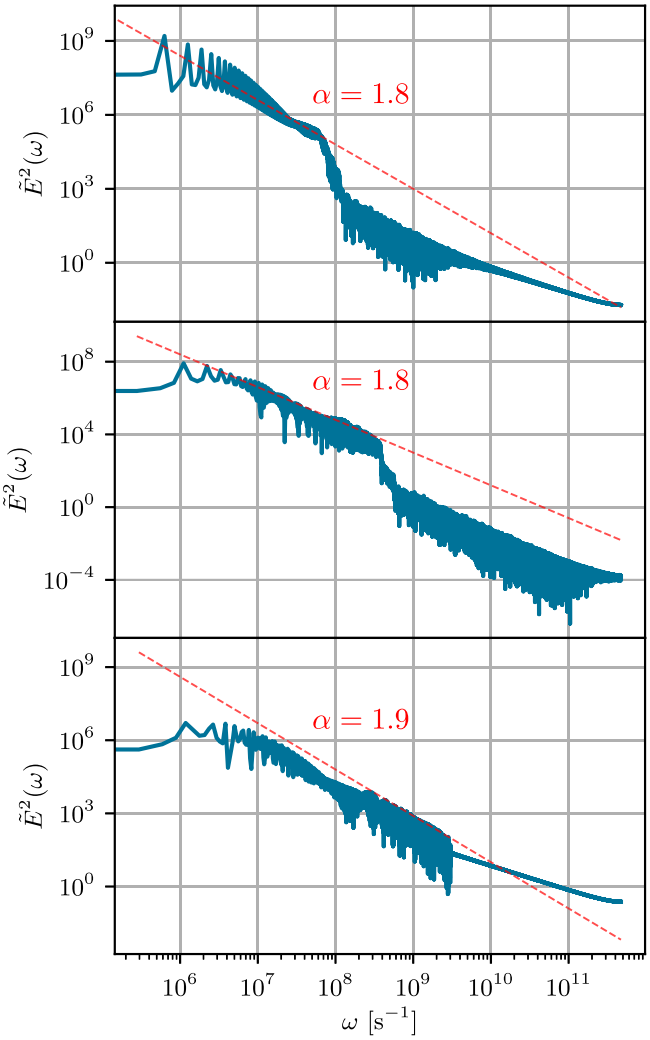

Figure 4. The power spectra of the electric field $\tilde{E}^2$ for a time interval that corresponds to four pair production limit cycles. The different plots correspond to different values of the pair production parameter: $g = 10^{-11}$ (top), $g = 10^{-10}$ (middle), and $g = 10^{-9}$ (bottom). The dotted lines are simple estimates of the spectral indices. The spectral index is only weakly dependent on the pair production rate, but the frequency cutoff depends sensitively on the parameter g.

Cruz et al. (2021). Such a comparison will not only check the validity of this model, but also provide a guide for choosing the parameters, potentially allowing for extrapolation to realistic pulsars. Such a study will be the focus of a future work.

Our time-dependent pair production model not only describes $e^{\pm}$ discharge at the pulsar polar cap, but should also be applicable to other systems where a spark gap is expected, e.g., the twisted flux tubes of a magnetar (e.g., Beloborodov 2013) or black hole magnetospheres (e.g., Chen et al. 2018). For other systems, the pair production term may need to be modified accordingly, but the set of Equations (15)–(18) should generally remain unchanged.

We have introduced a few simplifying assumptions to make the problem tractable. One of the most significant was replacing $\langle 1/\gamma^3 \rangle$ in Equation (16) by $1/\langle \gamma \rangle^3$, which closes the equations but significantly underestimates the value of this term. For example, previous studies have found that when abundant secondary pairs are present, the expectation value $\langle 1/\gamma^3 \rangle$ becomes close to $1/\langle \gamma \rangle$ (see, e.g., Gedalin et al. 1998; Cruz et al. 2021). Moreover, our pair production source term is rather crude, allowing pair production from all particles at a rate proportional to their energies. As a result, the number densities $n_{\pm}$ from the model are much higher than what was generally predicted by more sophisticated theoretical and numerical models of the pair production process (e.g., Timokhin & Harding 2019). To improve the estimates of $n_{\pm}$, more moments such as $\langle p_{\pm}^2 \rangle$ can be included in the equations as discussed in Appendix A. However, more detailed modeling of the pair production term will also be needed in order to yield a more reliable prediction. Nevertheless, our results share common features with those obtained by PIC simulations. The behavior of electric current (Figure 1) closely resembles what was seen in simulations by Timokhin (2010). A direct quantitative comparison with existing PIC simulation results is more challenging, since we have made simplifying

assumptions on both the pair production model and the plasma escape mechanism.

Another limitation of this model is that it assumes local feedback of pair production on the electric field, which may not be realistic due to finite photon free paths. In the case of nonlocal pair production, a zero-dimensional model such as proposed in this paper is likely no longer applicable. Further comparison with direct numerical simulations should be able to measure the effect of nonlocal electric field screening and find the parameter regimes where local pair production is a good approximation.

Despite all its limitations, we believe this model elucidates some of the most important features of the pair cascade process. In addition, this model can potentially provide a powerful way to compute the time dependence of parallel electric field $\boldsymbol{E}\cdot\boldsymbol{B}$ in pair-producing regions in the pulsar magnetosphere over a long period of time. Such a calculation can be used to estimate the production rate of ALPs and their spectra. Tracing the propagation of ALPs and their conversion back to photons can potentially give more stringent constraints on their allowable parameter space than what is currently available.

Acknowledgments

We thank Yajie Yuan, Anatoly Spitkovsky, Sam Witte, Anirudh Prabhu, and James Buckley for helpful discussions and comments on the manuscript. We also thank the anonymous referee for the comments that improved the manuscript A.C. is supported by NSF grants DMS-2235457 and AST-2308111. T.O. is supported by the U.S. Department of Energy under grant No. DE-SC 0017987.

Appendix A
Computing the Expectation Value $\langle 1/\gamma^3\rangle$

In the main text, we have made the bold assumption that $\langle 1/\gamma^3\rangle \approx 1/\langle\gamma\rangle^3$ in order to close the set of Equations (15)–(18). In this appendix, we attempt to justify our assumption and outline a systematic way to improve this estimate. We can actually expand $1/\gamma^3$ around the expectation value $\gamma = \langle\gamma\rangle$:

$$\frac{1}{\gamma^3} = \frac{1}{\langle\gamma\rangle^3} - \frac{3}{\langle\gamma\rangle^4}(\gamma - \langle\gamma\rangle) + \frac{6}{\langle\gamma\rangle^5}(\gamma - \langle\gamma\rangle)^2 + \ldots \quad \text{(A1)}$$

This is an asymptotic expansion that may not be convergent, but it still provides us with a systematic way to approximate the expectation value of $1/\gamma^3$ by truncating the series at the desired order. Taking the expectation value of Equation (A1), the first-order term goes to zero, and we have

$$\left\langle \frac{1}{\gamma^3} \right\rangle = \frac{1}{\langle\gamma\rangle^3} + \sum_{n=2}^{\infty}(-1)^n \frac{(n+1)(n+2)}{2\langle\gamma\rangle^{n+3}}\langle(\gamma - \langle\gamma\rangle)^n\rangle. \quad \text{(A2)}$$

Therefore, our assumption in the main text is equivalent to only keeping the zeroth-order term in this expansion. This assumption is reasonable during the phase of electric field growth, where all electrons and positrons are accelerated together and the distribution function has little spread, but it significantly underestimates $\langle 1/\gamma^3\rangle$ when pair production has begun and the electric field is screened, as shown by Cruz et al. (2021) and Tolman et al. (2022).

We can improve the estimate by including more terms in the expansion. For example, if we truncate Equation (A2) at $n = 2$, the result becomes

$$\left\langle \frac{1}{\gamma^3} \right\rangle = \frac{1}{\langle\gamma\rangle^3} + \frac{6}{\langle\gamma\rangle^5}(\langle\gamma^2\rangle - \langle\gamma\rangle^2). \quad \text{(A3)}$$

At large γ, $\langle\gamma^2\rangle \approx \langle p^2\rangle$, for which we can write down an evolution equation:

$$\begin{aligned}\frac{\partial\langle p^2\rangle}{\partial t} &= -\frac{\dot{n}}{n^2}\int p^2 f\, dp + \frac{1}{n}\int p^2\frac{\partial f}{\partial t}\, dp \\ &= -\frac{\dot{n}}{n}\langle p^2\rangle - \frac{c}{L}\langle p^2\rangle + 2qE\langle p\rangle + \frac{1}{n}\int p^2 S\delta(p)dp \\ &= -\frac{S}{n}\langle p^2\rangle + 2qE\langle p\rangle, \end{aligned} \quad \text{(A4)}$$

where we have assumed that pairs are produced at $p = 0$, as was done in the main text. If we assume a nonzero but equal and opposite $\pm p_{\rm pair}$, then the higher moments will contain $p_{\rm pair}$ as a parameter. This equation shows that the time evolution of higher moments of the distribution function depends on lower moments, and we can repeat this procedure as needed up to nth order in Equation (A2).

Figure 5 shows a comparison between the solutions with the zeroth-order closure used in the main text and the second-order closure defined by Equation (A3), with all parameters identical. The overall qualitative features of the solution remain similar, but the second-order closure solution has an overall lower $\bar{\omega}$. It mainly achieves this by having a lower $n_{\pm}$. We expect that including more moments in the expansion will generally lead to

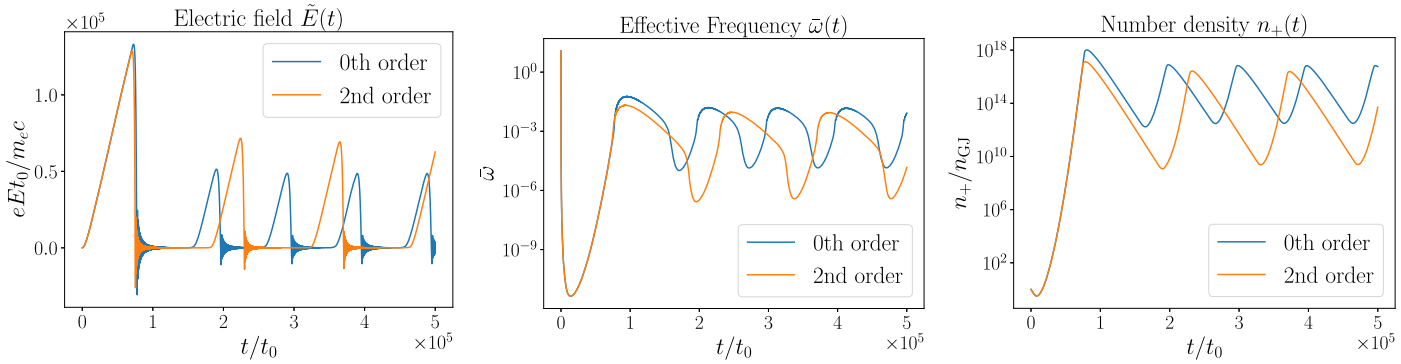

Figure 5. Comparison of the solution with different closure schemes. Blue curves show the solution with $\langle 1/\gamma^3\rangle = 1/\langle\gamma\rangle^3$, while orange curves show the solution with the second-order closure defined by Equation (A3).

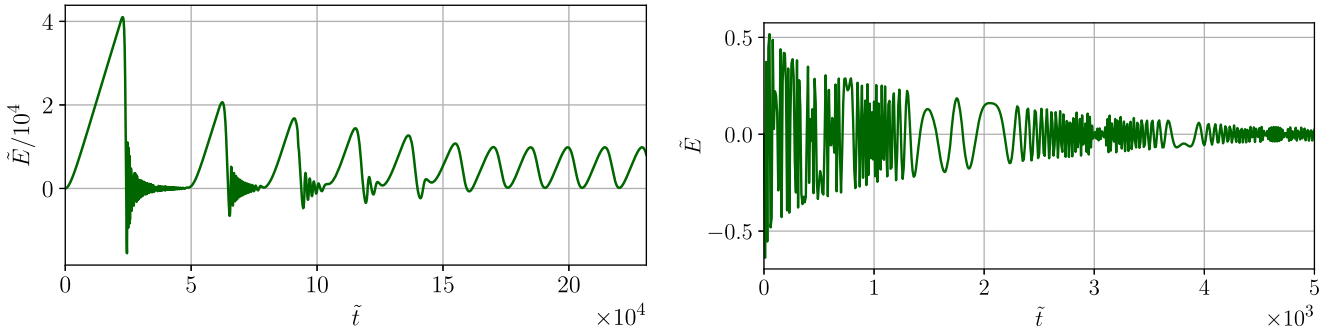

Figure 6. Plots of the electric field evolution obtained by two different models of the pair production source function. The left and right panels assume $\tilde{S} = g\,|\tilde{E}|\sum_s \tilde{n}_s$ and $\tilde{S} = g\sum_s |\langle \tilde{p}_s \rangle|$, respectively. All initial conditions and values of parameters are the same as in the reference model except for the efficiency of charged particle production rate g: $g = 10^{-7}$ (left) and $g = 10^{-3}$ (right).

a more realistic number density. Such a study is beyond the scope of this paper and will be deferred to future works.

Appendix B
Alternative Pair Production Models

Among six models proposed in the main text, only $\tilde{S} = g\sum_s \tilde{n}_s |\langle p_s \rangle|$ reproduces the limit-cycle behavior of electric fields. The other five models were not sufficient to yield this behavior (see Figure 6 for some examples) with reasonable values of initial condition and parameters. Below we briefly describe where each of the other five models was unsuccessful in reproducing the limit cycle.

1. $\tilde{S} = g$;
   In this case, Equation (17) predicts that the deviation of the plasma density from its critical value $\tilde{n}_\pm = \tilde{L}g$ is exponentially suppressed as a function of time. The number density of charged particles in this model ends up being nearly constant.
2. $\tilde{S} = g\sum_s \tilde{n}_s$;
   Depending on the sign of the right-hand side of Equation (17), the plasma density endlessly either grows or drops regardless of the behaviors of the electric fields, the charged current, and the averaged momentum.
3. $\tilde{S} = g\sum_s |\langle \tilde{p}_s \rangle|$;
   See Figure 6, right panel. Numerical simulations have shown that the averaged momentum tends to be relaxed to a constant value. Then, the plasma density also reaches a constant value, similar to the $\tilde{S} =$ constant case. The electric field never grows appreciably.
4. $\tilde{S} = g|\tilde{E}|$;
   With this form of the source term $\tilde{S}$, the averaged momentum of electrons continues to decrease. That of positrons is monotonically increased or decreased depending on the value of g.
5. $\tilde{S} = g|\tilde{E}|\sum_s \tilde{n}_s$;
   See Figure 6, left panel. A limit cycle tries to form but settles to an oscillation that is different in nature. In addition, Equation (18) has a particular solution in this model: $\langle \tilde{p}_s \rangle = q_\pm/eg$. Thus, this model cannot describe the acceleration/deceleration of charged particles due to the electric fields.

ORCID iDs

Takuya Okawa https://orcid.org/0009-0003-9478-380X
Alexander Y. Chen https://orcid.org/0000-0002-4738-1168

References

Abbott, L. F., & Sikivie, P. 1983, PhLB, 120, 133
Arons, J. 1983, ApJ, 266, 215
Bai, X.-N., & Spitkovsky, A. 2010, ApJ, 715, 1282
Bates, S. D., Lorimer, D. R., & Verbiest, J. P. W. 2013, MNRAS, 431, 1352
Beloborodov, A. M. 2008, ApJL, 683, L41
Beloborodov, A. M. 2013, ApJ, 777, 114
Chen, A. Y., Yuan, Y., & Yang, H. 2018, ApJL, 863, L31
Cheng, K. S., Ho, C., & Ruderman, M. 1986, ApJ, 300, 500
Contopoulos, I., Kazanas, D., & Fendt, C. 1999, ApJ, 511, 351
Cruz, F., Grismayer, T., Chen, A. Y., Spitkovsky, A., & Silva, L. O. 2021, ApJL, 919, L4
Cruz, F., Grismayer, T., & Silva, L. O. 2021, ApJ, 908, 149
Daugherty, J. K., & Harding, A. K. 1983, ApJ, 273, 761
Dine, M., & Fischler, W. 1983, PhLB, 120, 137
Gedalin, M., Melrose, D. B., & Gruman, E. 1998, PhRvE, 57, 3399
Goldreich, P., & Julian, W. H. 1969, ApJ, 157, 869
Gralla, S. E., Lupsasca, A., & Philippov, A. 2017, ApJ, 851, 137
Hairer, E., Nørsett, S., & Wanner, G. 1993, Solving Ordinary Differential Equations II: Stiff and Differential-Algebraic Problems (Berlin: Springer)
Jackson, J. D. 1999, Classical Electrodynamics (College Park, MD: American Association of Physics Teachers)
Levinson, A., Melrose, D., Judge, A., & Luo, Q. H. 2005, ApJ, 631, 456
Noordhuis, D., Prabhu, A., Witte, S. J., et al. 2023, PhRvL, 131, 111004
Philippov, A., & Kramer, M. 2022, ARA&A, 60, 495
Philippov, A., Timokhin, A., & Spitkovsky, A. 2020, PhRvL, 124, 245101
Prabhu, A. 2021, PhRvD, 104, 055038
Preskill, J., Wise, M. B., & Wilczek, F. 1983, PhLB, 120, 127
Ruderman, M. A., & Sutherland, P. G. 1975, ApJ, 196, 51
Spitkovsky, A. 2006, ApJL, 648, L51
Sturrock, P. A. 1971, ApJ, 164, 529
Timokhin, A. N. 2010, MNRAS, 408, 2092
Timokhin, A. N., & Arons, J. 2013, MNRAS, 429, 20
Timokhin, A. N., & Harding, A. K. 2019, ApJ, 871, 12
Tolman, E. A., Philippov, A. A., & Timokhin, A. N. 2022, ApJL, 933, L37